

FINAL
11-34-92
OOT

40143

Multigrid Computations of 3-D Incompressible Internal and External Viscous Rotating Flows

By

*Chunhua Sheng, Lafayette K. Taylor
Jen-Ping Chen, Min-Yee Jiang and
David L. Whitfield*



*Computational Fluid Dynamics Laboratory
NSF Engineering Research Center for Computational Field Simulation*

February 1996

MSSU-EIRS-ERC-96-1

*Mississippi State University
P.O. Box 6176
Mississippi State, MS 39762*

Multigrid Computations of 3-D Incompressible Internal and External Viscous Rotating Flows

By

*Chunhua Sheng, Lafayette K. Taylor,
Jen-Ping Chen, Min-Yee Jiang and
David L. Whitfield*



*Computational Fluid Dynamics Laboratory
NSF Engineering Research Center for Computational Field Simulation
February 1996*

MSSU-EIRS-ERC-96-1

*Mississippi State University
P.O. Box 6176
Mississippi State, MS 39762*

Table of Contents

	Page
Acknowledgements	ii
Abstract	iii
I. Introduction	1
II. Governing Equations	3
III. Numerical Solution Method	5
IV. Multigrid Method	7
V. Results	8
VI. Conclusions	13
References	14

Acknowledgement

This research was sponsored by the NASA Lewis Research Center, Cleveland, Ohio under NASA Grant NAG 3-1357. Joe Veres was the technical monitor at the beginning of this effort and Margaret Proctor is the current technical monitor. This support is gratefully acknowledged. The authors also wish to express their appreciation to Collin Pardue for generating the fine grid for the NASA LSCC.

Abstract

This report presents multigrid methods for solving the 3-D incompressible viscous rotating flows in a NASA low-speed centrifugal compressor and a marine propeller 4119. Numerical formulations are given in both the rotating reference frame and the absolute frame. Comparisons are made for the accuracy, efficiency, and robustness between the steady-state scheme and the time-accurate scheme for simulating viscous rotating flows for complex internal and external flow applications. Prospects for further increase in efficiency and accuracy of unsteady time-accurate computations are discussed.

I. Introduction

Computation of unsteady rotating flows can be applied in many practical areas such as in turbomachinery cascade flow, helicopter rotor flow, and marine propulsor flow predictions[1][2][3]. Two numerical approaches are typically used in the simulation of unsteady flows in rotating machinery. A common way is to solve the governing equations in a rotating reference frame by computing either the relative velocity [4] or the absolute velocity [2][5]. The advantage of this approach is that it uses a steady-state formulation, if the flow field can be viewed as a steady state in the rotating frame. Thus, many efficient acceleration techniques, such as local time stepping and multigrid method, can be used. An alternative to the steady-state approach is to establish the governing equations in a fixed absolute frame, and solve the equations using a time-accurate formulation. However, the demand on accuracy and efficiency for time-accurate solutions is much higher than that for steady-state solutions. For the reason of accuracy, time step is restricted, and it has to be chosen smaller than the smallest characteristic scale length to be resolved. The restriction on the time step reduces the efficiency of implicit schemes, but it is the most straightforward way to deal with the general unsteady flows that can not be viewed as a steady state in the rotating reference frame, such as the unsteady rotor/stator interaction.

This report describes and compares both numerical formulations of solving the governing equations in the rotating reference frame with a steady-state method and in the absolute frame with an unsteady time-accurate method. In the rotating frame, a steady relative velocity flow field is pursued. In order to fully use the original code which is written in the absolute velocity components, a dependent variable transformation is first performed to change the relative velocity components into the absolute velocity components in the governing equations, and the computation is performed based on absolute velocity instead of relative velocity in the rotating frame [2][5]. Two practical applications are presented for solving viscous rotating flows in a NASA low-speed centrifugal compressor and in a marine propeller 4119. The purpose here is to evaluate and validate the accuracy,

efficiency and robustness of the current method to predict complex flow fields for both internal and external flow applications.

In the following, the 3-D incompressible Navier–Stokes equations in general curvilinear coordinates are first given, followed by the numerical methods used to solve the equations in both the rotating reference frame and absolute frame. The difference between the two approaches is addressed. Then the multigrid implementation [6][7] is illustrated to accelerate the solutions in both the rotating and absolute frames. Computational results of viscous rotating flows in both impeller and propeller cases are presented. In the last section, some conclusions are given.

II. Governing Equations

The artificial compressibility form of the 3-D incompressible Navier–Stokes equations in a general curvilinear coordinate system (ξ, η, ζ, τ) , which rotates about the x -axis at a constant speed of Ω , can be written as follows

$$\frac{\partial Q}{\partial \tau} + \frac{\partial F}{\partial \xi} + \frac{\partial G}{\partial \eta} + \frac{\partial H}{\partial \zeta} = S \quad (1)$$

where Q , the flux vectors F , G , H and the source term S are

$$Q = J \begin{bmatrix} p \\ u \\ v \\ w \end{bmatrix} \quad S = J \begin{bmatrix} 0 \\ 0 \\ -\Omega w \\ \Omega v \end{bmatrix}$$

$$F = J \begin{bmatrix} \beta(U' - \xi_t) \\ uU' + \xi_x p - \tilde{T}_{\xi_x} \\ vU' + \xi_y p - \tilde{T}_{\xi_y} \\ wU' + \xi_z p - \tilde{T}_{\xi_z} \end{bmatrix}$$

$$G = J \begin{bmatrix} \beta(V' - \eta_t) \\ uV' + \eta_x p - \tilde{T}_{\eta_x} \\ vV' + \eta_y p - \tilde{T}_{\eta_y} \\ wV' + \eta_z p - \tilde{T}_{\eta_z} \end{bmatrix}$$

$$H = J \begin{bmatrix} \beta(W' - \zeta_t) \\ uW' + \zeta_x p - \tilde{T}_{\zeta_x} \\ vW' + \zeta_y p - \tilde{T}_{\zeta_y} \\ wW' + \zeta_z p - \tilde{T}_{\zeta_z} \end{bmatrix}$$

Here J , p , u , v , and w denote the Jacobian transformation, pressure, and the Cartesian velocity components in the absolute frame, respectively. β is the artificial compressibility coefficient, and terms \tilde{T}_{k_x} , \tilde{T}_{k_y} , \tilde{T}_{k_z} , where $k=\xi, \eta$, and ζ , are the viscous flux components in curvilinear coordinates. The Baldwin–Lomax algebraic turbulence model is adopted in this work. The relative contravariant velocity components U' , V' , and W' are defined as

$$U' = \xi_x u' + \xi_y v' + \xi_z w' + \xi_t$$

$$V' = \eta_x u' + \eta_y v' + \eta_z w' + \eta_t$$

$$W' = \zeta_x u' + \zeta_y v' + \zeta_z w' + \zeta_t$$

where u' , v' , and w' are the relative velocity components in the rotating reference frame, and are written in terms of absolute velocity components u , v , and w as

$$u' = u \quad v' = v - \Omega z \quad w' = w + \Omega y$$

To solve the governing equations in an absolute frame, one can simply set the rotating speed Ω to zero in the above equations and evaluate ξ_t , η_t , and ζ_t as a result of grid rotation, which reduces to the normal conservative form of 3-D incompressible Navier–Stokes equations in general curvilinear coordinates based on the fixed absolute frame. Grid speeds have been included in the above formulation to allow grid motion relative to both the rotating and the absolute frame. In this work, however, only steady state solutions with stationary grids are pursued in the rotating frame. These steady state solutions of the absolute velocity on stationary grids in the rotating frame are carried out by setting Ω to the rotational speed and $\xi_t = \eta_t = \zeta_t = 0$ in Eq. (1). These absolute velocity solutions, which are viewed as steady state in the rotating frame, correspond to a particular time and position of the rotating grid in the absolute frame. The unsteady computations with dynamic grids are performed in the absolute frame.

III. Numerical Solution Method

In both the steady-state and unsteady formulations, the governing equations (1) are discretized by a cell centered finite-volume scheme. The time derivative is differenced using the Euler backward formula. For the one-dimensional case in both the rotating and the absolute frames (in the absolute frame, with the source term S equal to zero), it may be written as

$$\frac{Q_i^{n+1} - Q_i^n}{\Delta\tau} + \left(\bar{F}_{i+1/2}^{n+1} - \bar{F}_{i-1/2}^{n+1} \right) = S_i^{n+1} \quad (2)$$

where the index i corresponds to a cell center and indices $i \pm 1/2$ correspond to cell faces. The spatial discretization of the Euler fluxes at cell faces are approximated by using the third-order MUSCL approach in the Roe scheme. Details about this method can be found in [8].

The nonlinear system of equations (2) is solved by the discretized Newton-relaxation (DNR) method described in [9]. Note that Eq. (2) can be written in a simple form as

$$N(Q^{n+1}) = S^{n+1} \quad (3)$$

Applying Newton's method to Eq. (3) yields

$$N'(Q^{n+1,m})(Q^{n+1,m+1} - Q^{n+1,m}) = - (N(Q^{n+1,m}) - S^{n+1,m}) \quad (4)$$

where $m=1, 2, 3, \dots$ is the number of Newton iterations implemented at each time step, with $Q^{n+1,1} = Q^n$. These sub-iterations at each time level serve to eliminate linearization error, and thereby insure temporal accuracy. N' is the Jacobian matrix of the nonlinear equation (3) where the contribution of the source term is not included. The resulting formulation of Eq. (2) by Newton's method is

$$\begin{aligned}
& -\bar{F}'_{i-1/2, i-1} \Delta Q_{i-1}^{n+1, m} + \left(-\frac{I}{\Delta \tau} + \bar{F}'_{i+1/2, i} - \bar{F}'_{i-1/2, i} \right) \Delta Q_i^{n+1, m} + \bar{F}'_{i+1/2, i+1} \Delta Q_{i+1}^{n+1, m} \\
& = - \left[I_a \frac{Q_i^{n+1, m} - Q_i^n}{\Delta \tau} + \left(\bar{F}_{i+1/2}(Q^{n+1, m}) - \bar{F}_{i-1/2}(Q^{n+1, m}) \right) - S^{n+1, m} \right] \quad (5)
\end{aligned}$$

where \bar{F}' is the Jacobian matrix of the numerical flux vector \bar{F} , with the first subscript representing the position of the cell face of the numerical flux vector, and the second subscript representing the position of the dependent variable vector that the numerical flux vector is differentiated with respect to. I_a is an identity matrix except the first diagonal element is zero in order to satisfy the true incompressible continuity equation. In the rotating frame where the flow field is a steady state, continued iteration of Eq. (5) would presumably lead to $Q^{n+1} \rightarrow Q^n$. For unsteady computation in the absolute frame, time-dependent results can be achieved when a converged solution is obtained at each time step through Newton iterations. Gauss-Seidel relaxations are used to solve the linear system of equations, which results from Newton's method, approximately at each Newton iteration.

IV. Multigrid Method

In this work, the multigrid method [6][7] is used to accelerate both the steady-state and time-accurate computations. The difference between the steady and unsteady multigrid methods is that in the former, time is advanced in the fine grid as well as the coarse grid to achieve full efficiency. While in the later, both the fine grid and coarse grid equations must be solved at the same time level to ensure temporal consistency [10]. The two-level multigrid method for Eq. (3) can be briefly described as follows:

1. Iterate $N^h(Q^h)=S^h$ \mathcal{N} times on the fine grid h by Newton's method.
2. Restrict the residual and solution to the coarser grid $2h$, and iterate $N^{2h}(Q^{2h}) = S^{2h}$ \mathcal{N} times, where $S^{2h} = N^{2h}(I^{2h}_h Q^h) + R^{2h}_h(S^h - N^h Q^h)$ is the source term on the coarse grid $2h$.
3. Interpolate the correction from the coarser grid to the fine grid and update the solution $Q^h \leftarrow Q^h + P^{h}_{2h}(Q^{2h} - I^{2h}_h Q^h)$
4. Repeat steps 1~3 for \mathcal{M} times at the same time level, using Q^h as the new approximation to Q^{n+1} .

In the above procedure, \mathcal{N} is the number of Newton iterations for the fine grid and coarser grids, and \mathcal{M} is the number of multigrid cycles implemented at each time step. Choosing different values of \mathcal{N} and \mathcal{M} may form different multigrid strategies and result in different effects. In this work, the number of Newton iterations \mathcal{N} is chosen as one for all computations. The number of multigrid cycles \mathcal{M} used at each time step varies according to different cases. Note that if no coarser grids exist, both parameters \mathcal{M} and \mathcal{N} have the same meanings in regard to the implementation of the code.

V. Results

Two applications involving both internal and external viscous flows are presented here. One is a turbulent flow in a NASA low-speed centrifugal compressor (LSCC) [1]. Another case is a turbulent flow about a marine propeller 4119 [3]. In each case, computations were first performed by a steady numerical approach in the rotating frame, then compared with the unsteady time-accurate approach in the absolute frame. Computations were carried out on a single processor of an SGI 75MHz R8000 workstation.

A NASA Low-Speed Centrifugal Compressor

The study of the LSCC is sponsored by the NASA Lewis Research Center to evaluate the capability of the computational method to predict the flow field in the complex geometric channels of centrifugal compressors. The complex phenomena to be considered include secondary flows in the impeller passage, tip clearance flows, etc. The experimental investigation of the LSCC was conducted by Hathaway et al. in [1], which gives detail measurements of the velocity components V_r , V_t (V_θ in Ref.[1]), and V_x in the blade passage. These experimental data are used to verify the accuracy of computed results.

Two computational meshes for the LSCC geometry were built with about 300K and 200K grid points on the fine and coarse grids, respectively. The grid spacing on the fine grid surfaces is 4×10^{-6} , and has 73 points on the blade, 13 points on the tip clearance, 37 points spanwise, and 41 points pitch-wise (Figure 1). The Reynolds number is 4.3×10^6 , based on the velocity of the inlet flow and the diameter of the blade tip. The grid y^+ value on surfaces is about 1. The inflow boundary condition is given by specifying the three velocity components u , v , and w . The back pressure is specified at the exit of the computational domain. Figure 2 shows the convergence history of the steady-state solution in the rotating frame, based on the fine grid. A 3-level full coarsening multigrid strategy was employed to accelerate the convergence. A local time stepping was used with a maximum CFL number of 20. At each time step, only one multigrid cycle ($\mathcal{M}=1$), with 5 Gauss-Seidel relaxations

was implemented. The residual was reduced by 2 orders of magnitude in 200 multigrid cycles, and then became flat. The reason for that may be due to the extremely small volume in this fine grid (minimum volume is less than 1×10^{-14}). The computer requirement for this solution is 336 MB internal memory, and 27 hours of CPU time for 500 multigrid cycles on the machine mentioned above.

The following Figures 3(a) through 3(d) show computed and measured relative velocity components at 4 locations ($m/m_s=0.149, 0.475, 0.644,$ and 0.941 , where m/m_s is the non-dimensional shroud meridional distance) along the blade passage. The results in each plot are shown at every 5% of span, with the results nearest the shroud located at 95% of blade span from the hub, where 100% span denotes the blade tip. Agreement between the numerical prediction and the measurement is considered reasonably good. Figures 4(a) through (d) show computed particle traces on the suction and pressure surfaces, and the top and hub surfaces of the LSCC channels, based on the relative velocity. The plots indicate a continuing migration of fluid outward toward the tip near the blade surface (Figures 4 (a) and (b)).

The LSCC flow field was also solved based on the coarse mesh, using both the steady approach in the rotating frame and the unsteady time-accurate approach in the absolute frame. For the steady computation, the same multigrid strategy and parameters were employed as in the previous case. Figure 5 shows the convergence history in the coarse grid. A convergent solution was obtained in 500 multigrid cycles by reducing the residual for 4 orders of magnitude. The comparison of relative velocity components between the computation and experiment is very similar to the fine grid case (shown in Figures 3(a)~(d)), and therefore are not presented here. The unsteady calculation was started using local time stepping, and moving the entire grid at a rate of 300 time steps per revolution of the impeller. A 3-level multigrid procedure was also used to accelerate the convergence of the unsteady solution at each time step. After the solution marched for two revolutions, the calculation was switched to minimum time stepping, with 3000 time steps per revolution ($\Delta t=0.00029$). The final solution was obtained after about 4000 time iterations, due to the very small time step used in

the unsteady computation. The accuracy of the time-dependent solution will be discussed below. Another effort made by Taylor [11] using the Roe flux formulation (non-MUSCL type [12]) and a single grid approach showed similar results after about 6000 time step iterations of the unsteady computation. The cost of CPU time in these unsteady solutions is about 6~10 times that of the steady solution in the rotating frame.

The accuracy of time-dependent solutions is assessed with different time steps and multigrid cycles at each time step, by comparing with the results obtained using a steady approach in the rotating frame. The unsteady calculation can be performed at a larger time step of 300 cycles per revolution ($\Delta t=0.0029$), but the results differ from those obtained using the steady method, see Figure 6(a). Applying more multigrid iterations (M) at each time step seemed not to improve the solution very much, as shown in Figure 6(b). The accuracy of the unsteady solution is significantly improved only after reducing the time step to 0.00029, which is 3000 time steps per revolution (Figure 6). The above numerical results reveal the following characters of the code. First, the current unsteady code is robust, since the allowed time step is not bounded by numerics (stability), but by physics (resolution). Therefore, a largest possible time step can be selected in the computation to achieve best efficiency while maintaining desired accuracy. Second, one multigrid cycle is sufficient to provide a convergent solution at each time step in this case, since more iterations do not change the solution significantly. Third, the accuracy of time-accurate solutions is critically dependent on the time step used in the calculation, which suggests that higher order time accuracy may be preferred in unsteady computations, especially in complex internal flows. Though using a very large time step (or local time stepping) does not provide sufficient accuracy for the time-dependent solution, it is an efficient way to obtain an initial approximation to start with, or to quickly predict the flow field qualitatively. This strategy is also adopted in the computation of the next case.

A Marine Propeller 4119

There is reported computational result for the marine propeller 4119 [13]. The purpose here is to further assess the accuracy and efficiency of the current method for simulating external rotating

flows in a complex geometry. The computational grid consists of three blocks with a total of 280K points (Fig.7). There are 41 points in the streamwise and spanwise direction on the blade. The Reynolds number is 5.76×10^5 , based on the freestream velocity and the diameter of the blade. Figure 8 shows the convergence history of the steady solution obtained in the rotating frame, where the calculation was performed by using a 4-level multigrid full coarsening. At each time step, one multigrid iteration ($\mathcal{M}=1$), with 5 Gauss-Seidel relaxations was implemented. Local time stepping was used at a CFL number of 5. It is seen that the residual is reduced by about 3 orders of magnitude in 400 multigrid cycles. The CPU time of this calculation is about 20.6 hours on the SGI R8000 workstation.

The pressure coefficient distributions on the blade surface are shown in Figures 9(a)~(c), where r is the radial distance from the measured point on the blade to the hull axis, and R is the radius of blade tip. Favorable agreement was obtained between the computation and experiment, except for the pressure side at location $r/R=0.3$.

A computation was also performed using the unsteady time-accurate approach in the absolute frame. The initial solution was obtained by running the unsteady code in the absolute frame using local time stepping, while the computational grid was rotated at a rate of 200 cycles per revolution of the propulsor. After 200 time steps, the time-accurate calculation was started using a minimum time step of 0.004165, which is equivalent to 200 time steps per revolution. The multigrid cycles are employed to insure the convergence of the solution at each time step. It was found that the final solution with one multigrid cycle ($\mathcal{M}=1$) at each time step is close to that with two multigrid cycles ($\mathcal{M}=2$) at each time step. The unsteady solution became periodic after seven revolutions of the grid motion, or 1400 time steps. The cost of the CPU time of this unsteady solution is 3.5 times and 7 times that of the previous steady solution, with one and two multigrid cycles at each time step, respectively. Figures 10(a)~(c) show computed u -velocity contours obtained in the rotating frame and in the absolute frame with different multigrid cycles. Again, results obtained in the two different frames are similar. Figures 11(a)~11(c) show the computed and measured pressure coefficient dis-

tributions on the blade surface, where computed results were obtained in the absolute frame using 2 multigrid iterations at each time step. Computational results about thrust and torque coefficients are given in the Table 1. A desired accuracy is achieved in both computations.

VI. Conclusions

The computational results are presented for both internal and external viscous turbulent flows in complex geometries, a NASA low-speed centrifugal compressor and a marine propeller 4119. Computations are performed and compared in both the rotating reference frame using a steady-state formulation and the absolute frame using a time-accurate approach. A multigrid strategy is applied in both the steady-state and time-accurate computations to improve the efficiency and robustness of the algorithm. Results show that solving the unsteady rotating flow in a rotating frame costs much less CPU time than solving the flow in the absolute frame, in both internal and external flow cases. Comparison between the computed results and the experimental data is considered satisfactory for the current turbulence model and grid resolution.

Although the current multigrid algorithms are relatively efficient and robust, there are some unresolved issues which require further investigation. These include the use of a larger CFL number in the steady flow computations with a source term, and selection of the optimal time step for the best output regarding both accuracy and efficiency in time-dependent solutions. Finally, the second or higher order time difference scheme should be incorporated into the code to improve the accuracy and efficiency for time-accurate computations.

References

- [1] Hathway, M.D., Chriss, R.M., Wood, J.R., and Strazisar, A.J., "Experimental and Computational Investigation of the NASA Low-Speed Centrifugal Compressor Flow Field," *37th ASME International Gas Turbine Conference*, Cologne, Germany, June 1–4, 1992.
- [2] Agarwal, R.K., and Deese, J.E., "Euler Calculations for Flowfield of a Helicopter Rotor in Hover," *AIAA 4th Applied Aerodynamics Conference*, San Diego, California, June 7–11, 1986.
- [3] Stern, F., Zhang, D.H., Chen, B., and Kim, H.T., "Computation of Viscous Marine Propulsor Blade and Wake Flow," *Proc. 20th ONR Symposium on Naval Hydrodynamics*, Santa Barbra, CA, August 1994.
- [4] Choi, D. and Knight, C.J., "Computation of 3D Viscous Flows in Rotating Turbomachinery Blades," *AIAA-89-0323*, 27th Aerospace Sciences Meeting & Exhibit, January 9–12, 1989, Reno, NV.
- [5] Chima, R.V., and Yokota, J.W., "Numerical Analysis of Three-Dimensional Viscous Internal Flows," *AIAA Journal*, Vol. 28, No. 5, May 1990, pp. 798–806.
- [6] Sheng, C., Taylor, L.K., and Whitfield, D.L., "Multigrid Algorithm for Three-Dimensional Incompressible High-Reynolds Number Turbulent Flows," *AIAA Journal*, Vol. 33, No. 11., November 1995, pp. 2073–2079.
- [7] Sheng, C., Taylor, L.K., and Whitfield, D.L., "Multiblock Multigrid Solutions of Three-Dimensional Incompressible Turbulent Flows About Appended Submarine Configurations," *AIAA-95-0203*, January 1995.
- [8] Whitfield, D.L. and Taylor, L.K., "Numerical Solution of the Two-Dimensional Time-Dependent Incompressible Euler Equations," *Engineering and Industrial Research Station Report*, Mississippi State University, MSSU-EIRS-ERC-93-14, April 1994.

- [9] Vanden, K. and Whitfield, D.L., "Direct and Iterative Algorithms for the Three-Dimensional Euler Equations," *AIAA Journal*, Vol. 33, No. 5, May 1995, pp.851-858.
- [10] Sheng, C., Taylor, L.K., and Whitfield, D.L., "A Multigrid Algorithm for Unsteady Incompressible Euler and Navier-Stokes Flow Computations," *Proc. of Sixth International Symposium on Computational Fluid Dynamics*, Sept. 4-8, 1995, Lake Tahoe, NV.
- [11] Taylor, L.K., private communication, 1995.
- [12] Taylor, L.K. and Whitfield, D.L., "Unsteady Three-Dimensional Incompressible Euler and Navier-Stokes Solver for Stationary and Dynamic Grids," AIAA-91-1650, 22nd Fluid Dynamics Conference, June 24-26, 1991, Honolulu, Hawaii.
- [13] Jessup, S.D., "An Experimental Investigation of Viscous Aspects of Propeller Blade Flow," Ph.D. Dissertation, The Catholic University of America, 1989.

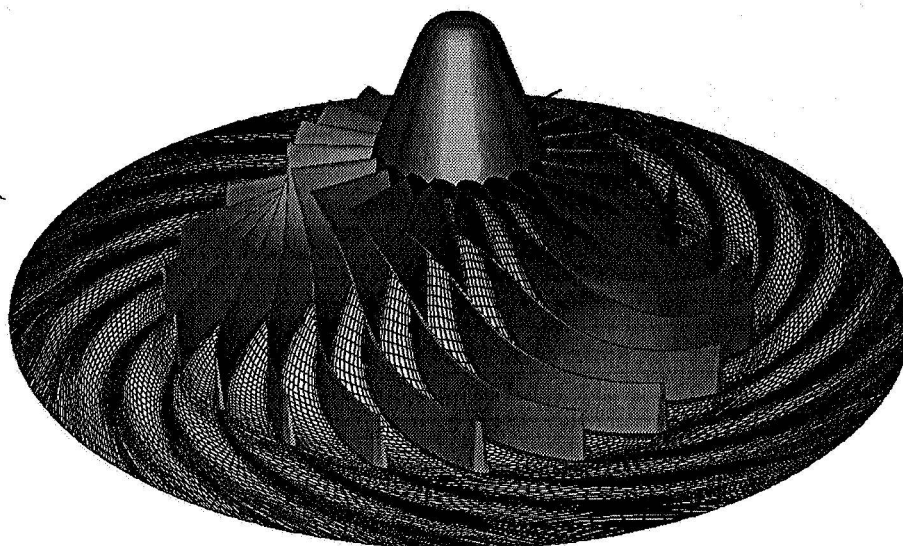


Figure 1 3-block grid of the NASA low-speed centrifugal compressor

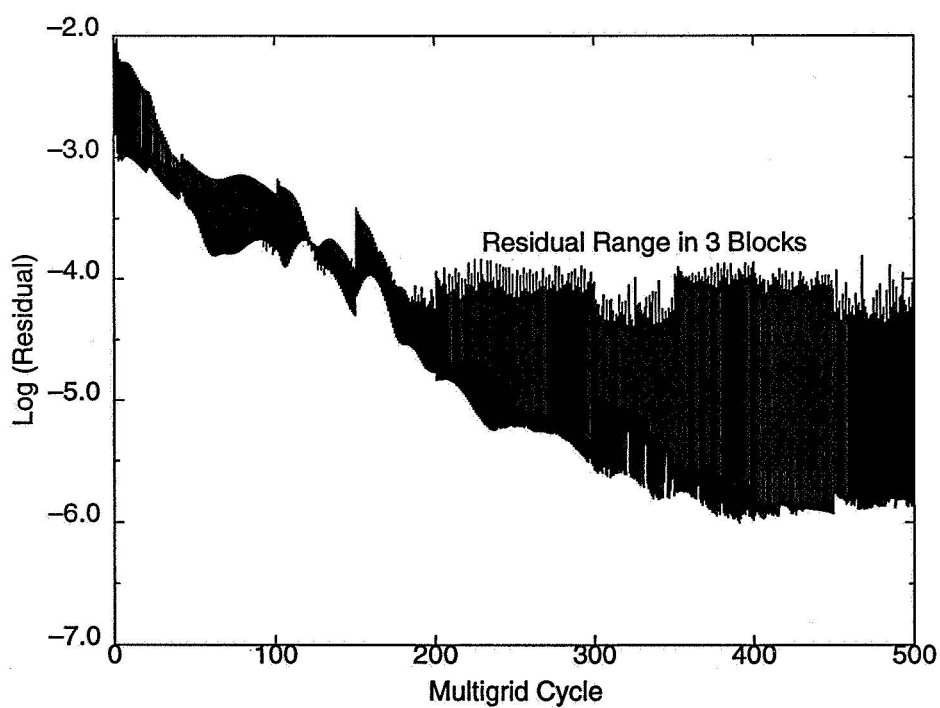


Figure 2 Fine grid convergence history of 3-level multigrid solution of the LSCC in rotating frame at CFL=20

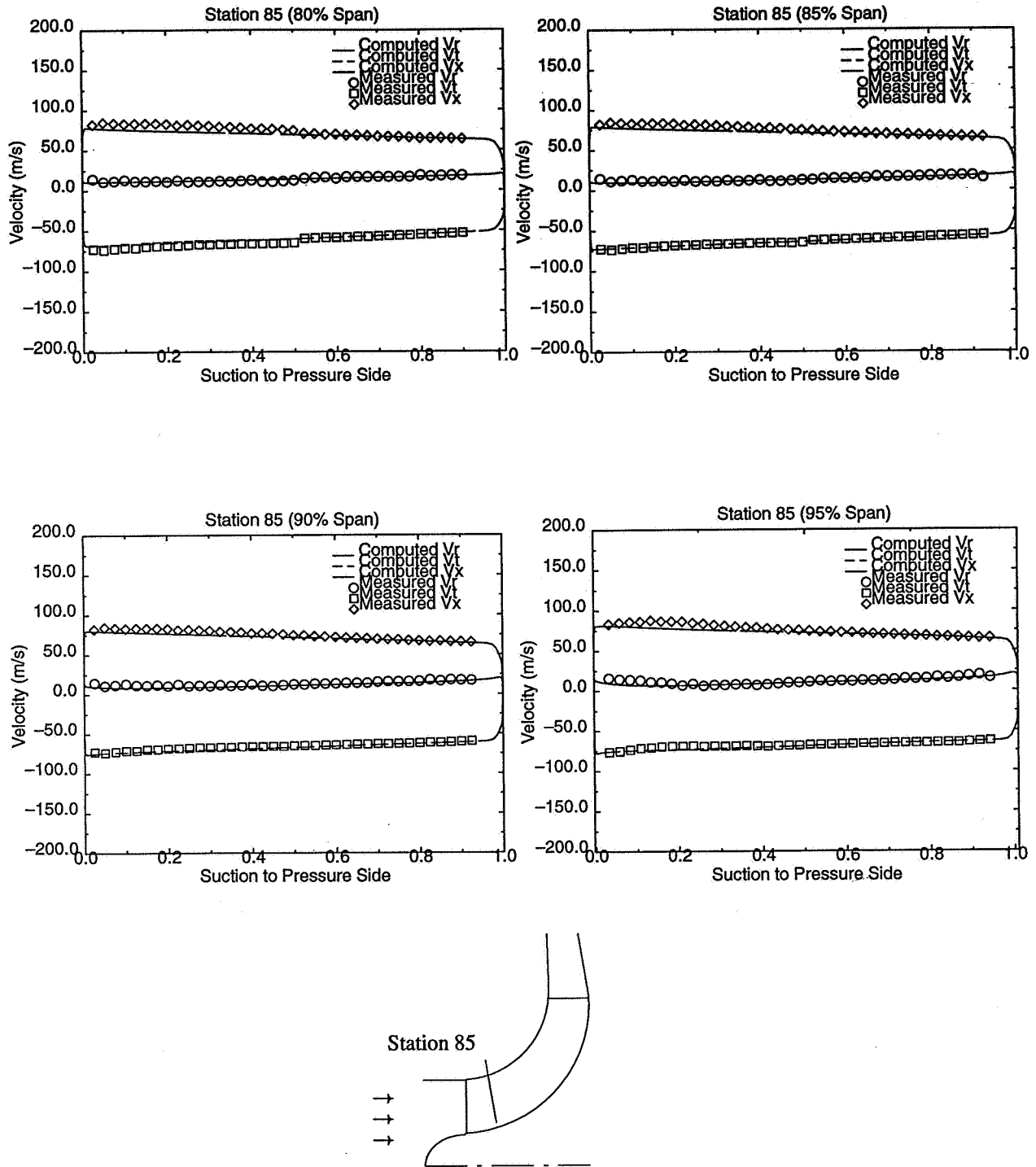


Figure 3 (a) Comparison of computed (in rotating frame) and measured relative velocity magnitude at station 85 ($m/m_s=0.149$)

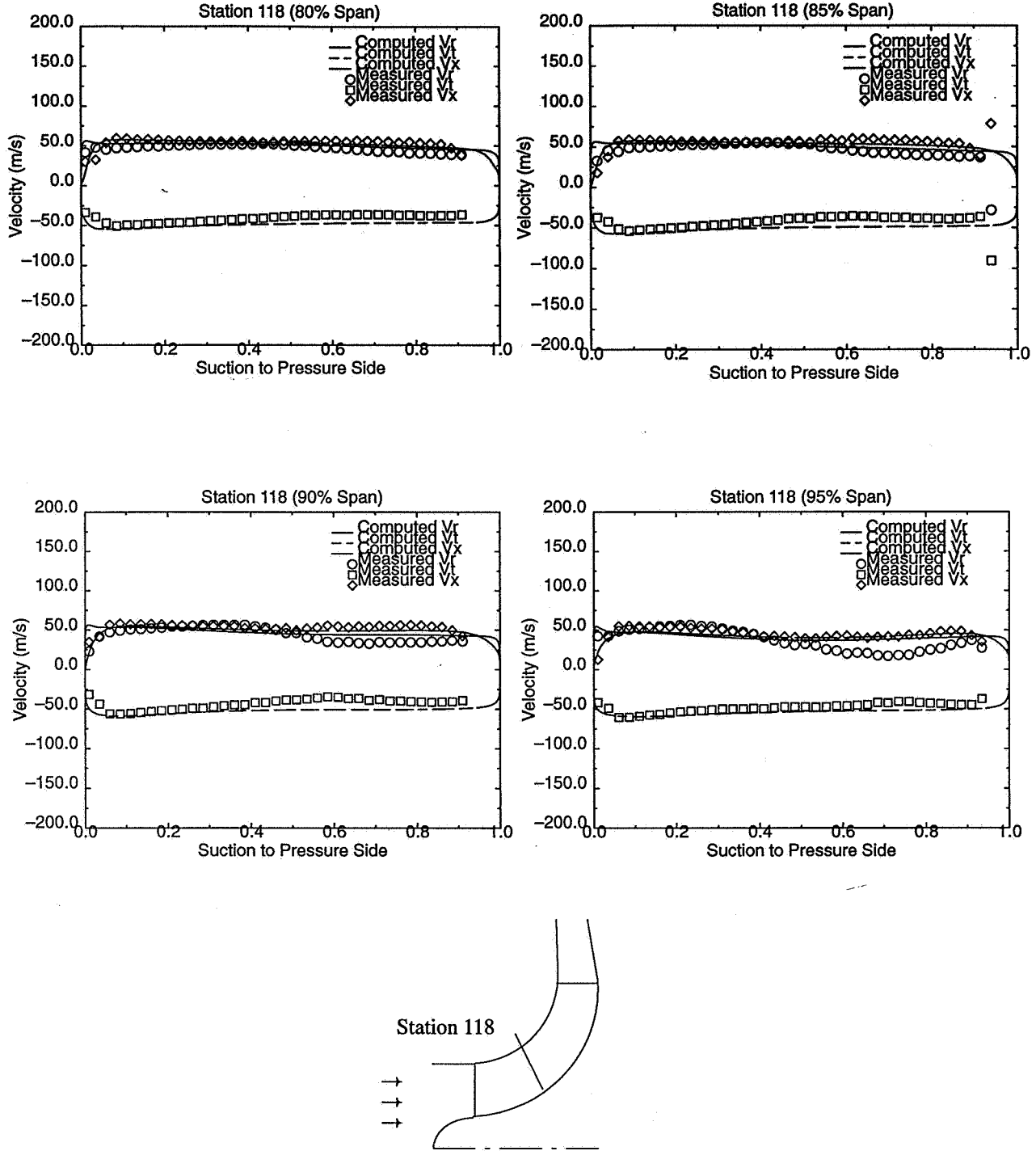


Figure 3 (b) Comparison of computed (in rotating frame) and measured relative velocity magnitude at station 118 ($m/m_s=0.475$)

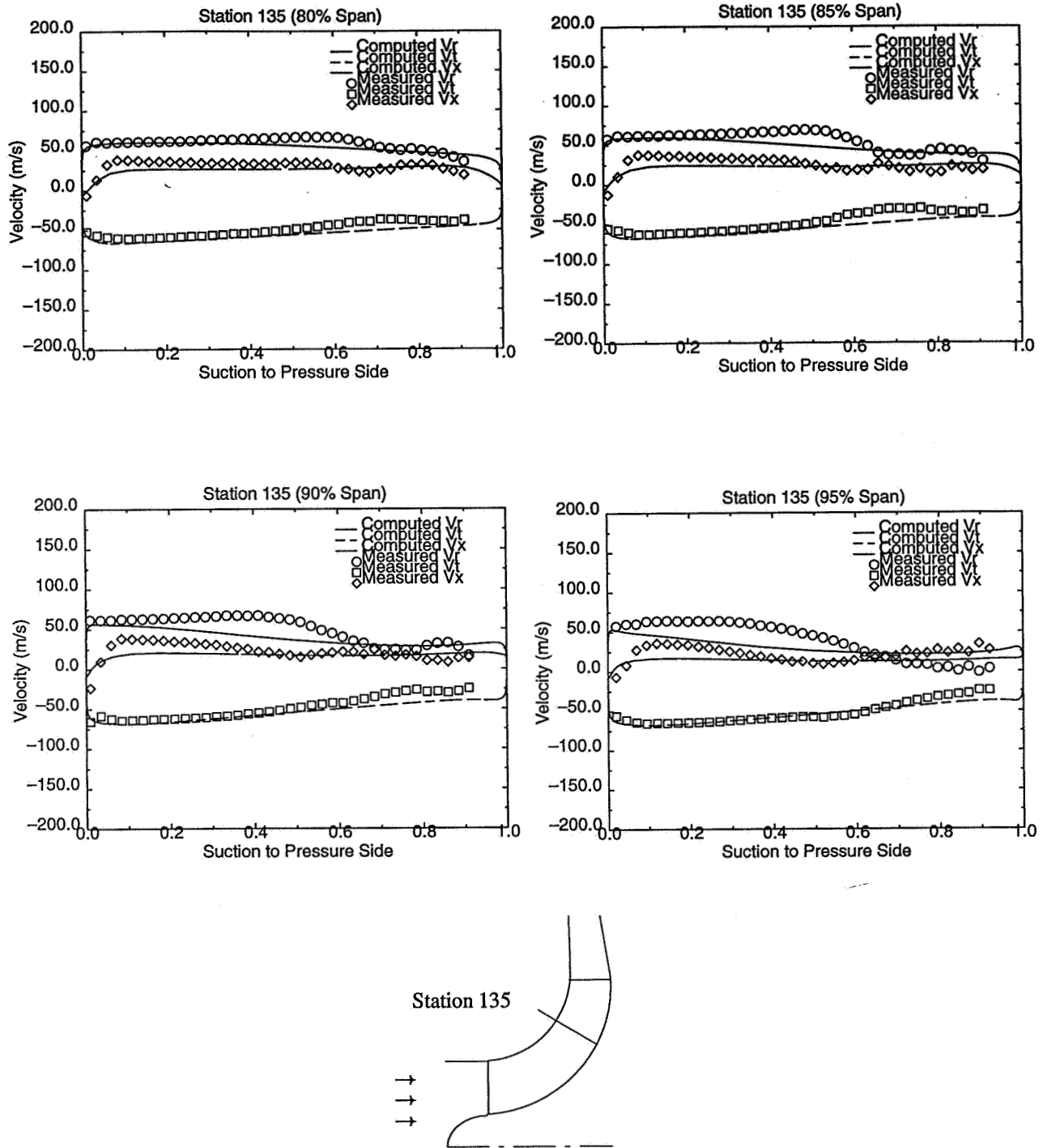


Figure 3 (c) Comparison of computed (in rotating frame) and measured relative velocity magnitude at station 135 ($m/m_s=0.644$)

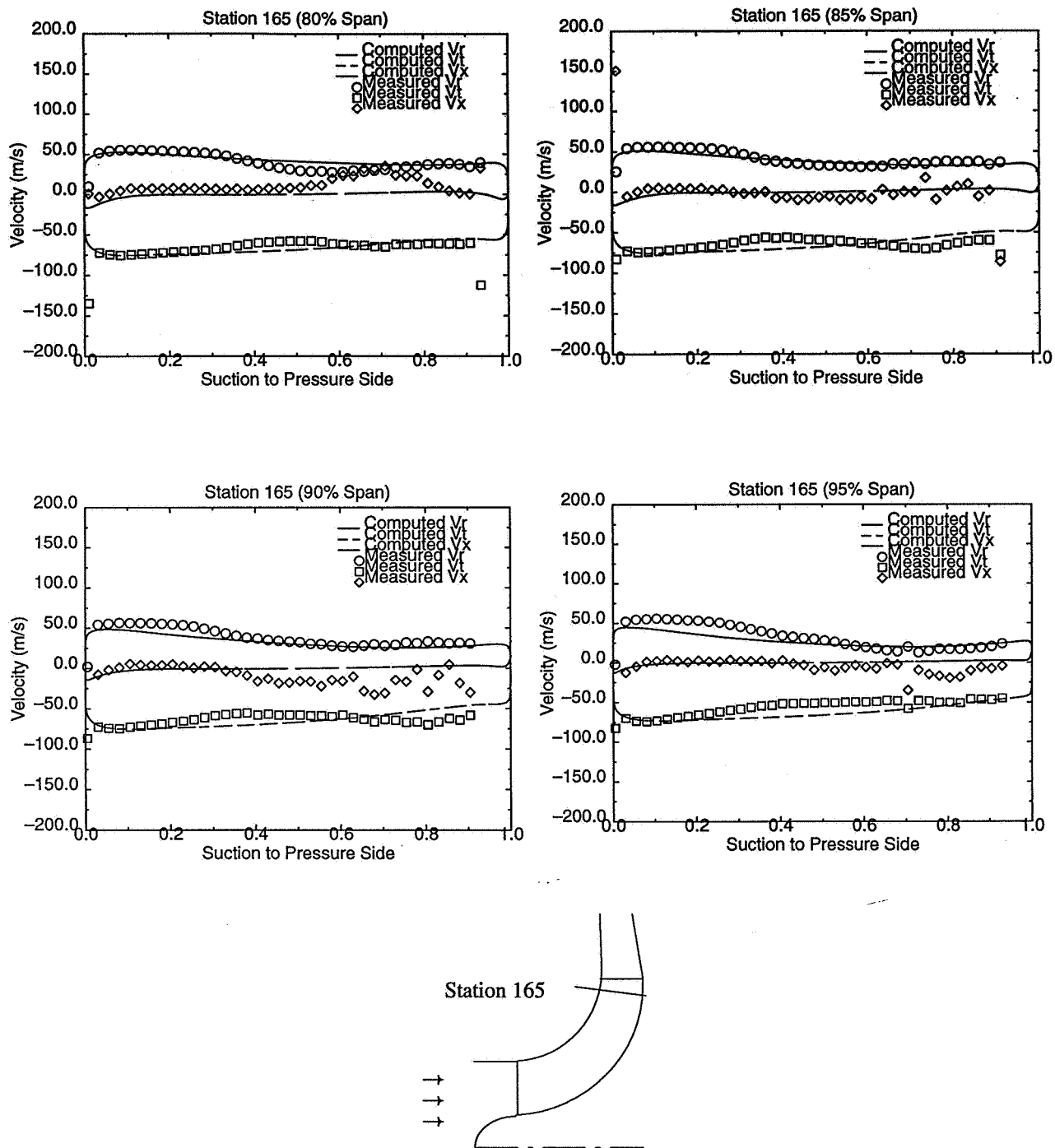
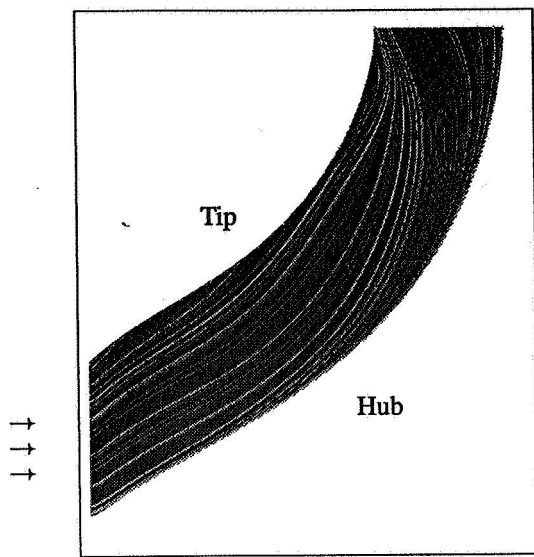
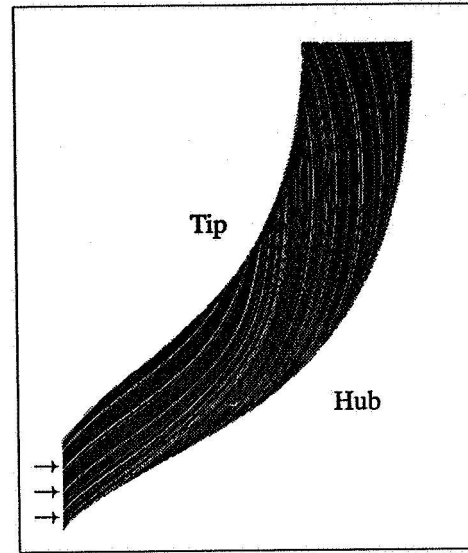


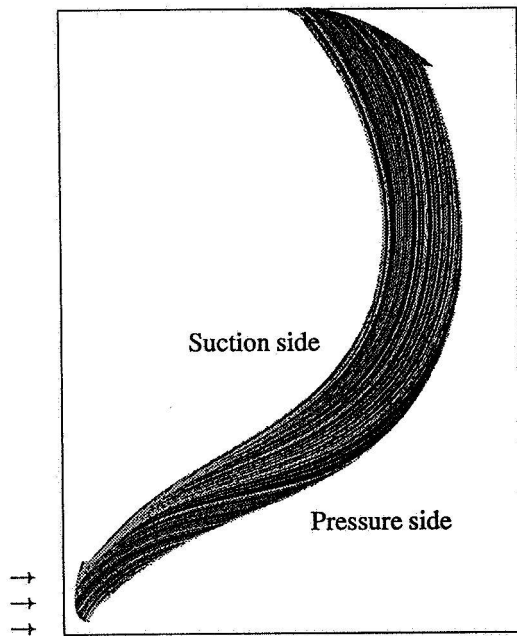
Figure 3 (d) Comparison of computed (in rotating frame) and measured relative velocity magnitude at station 165 ($m/m_s=0.941$)



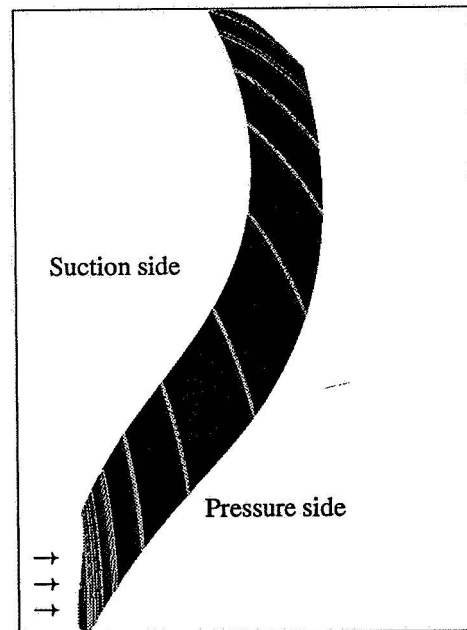
(a) Suction surface



(b) Pressure surface



(c) Hub surface



(d) Top surface

Figure 4 Particle traces on the surfaces of LSCC channel based on computed relative velocity

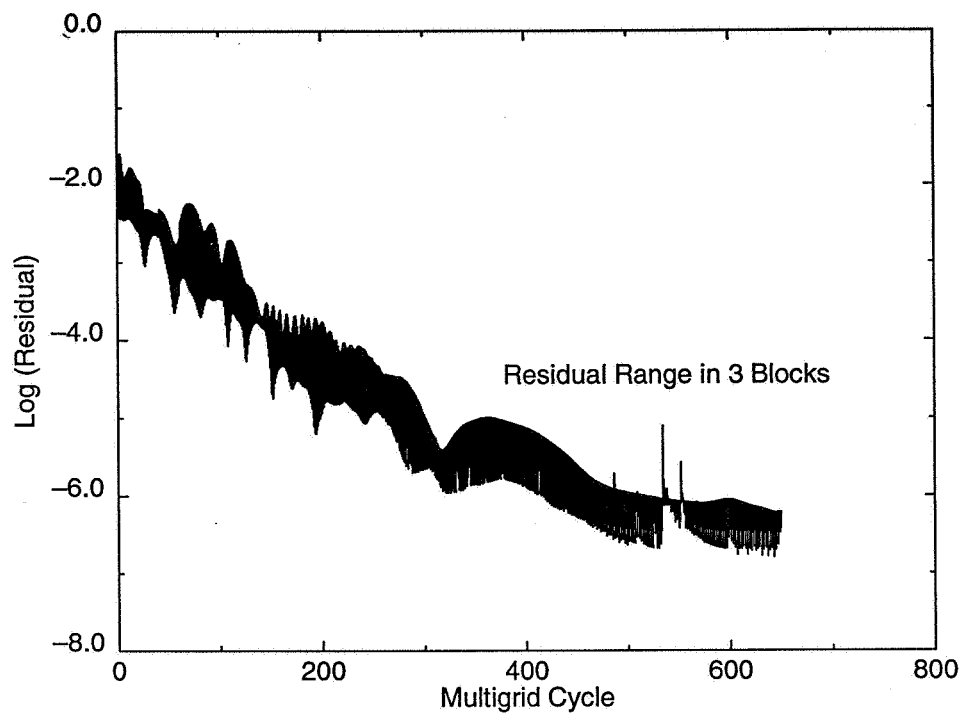


Figure 5 Coarse grid convergence history of 3-level multigrid solution of the LSCC in rotating frame at CFL=20

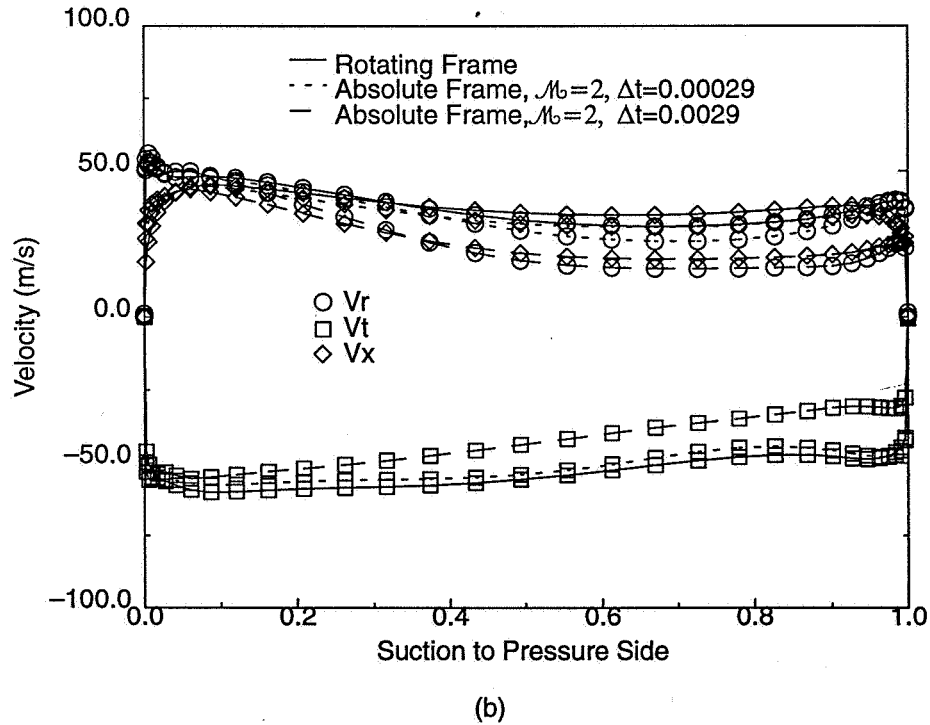
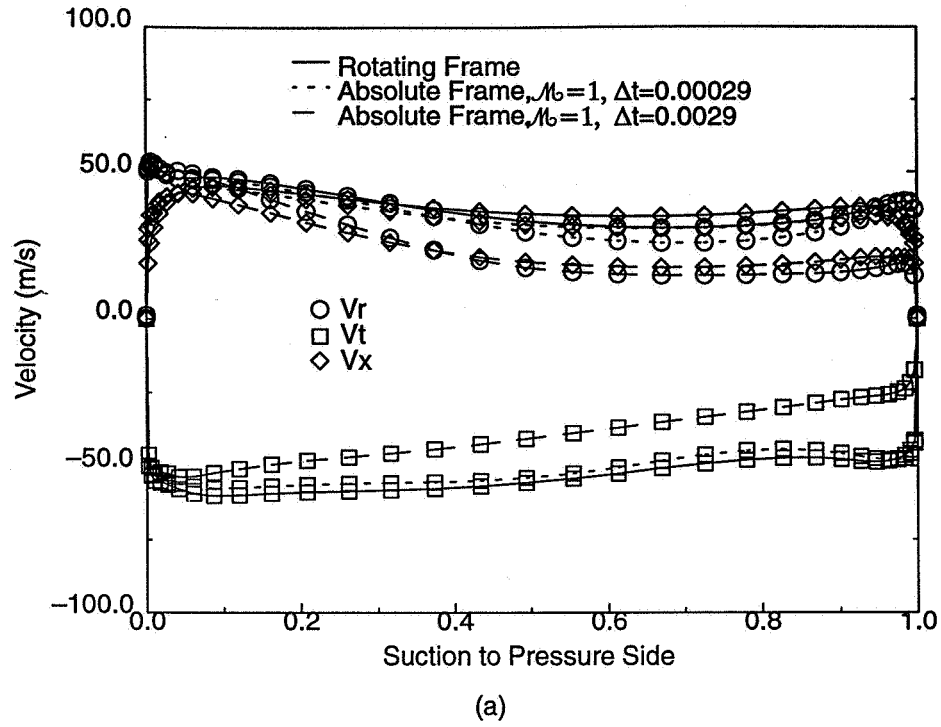


Figure 6 Comparison of computed velocity components at station 118 at 95% span at different multigrid cycles (M_b) and time steps

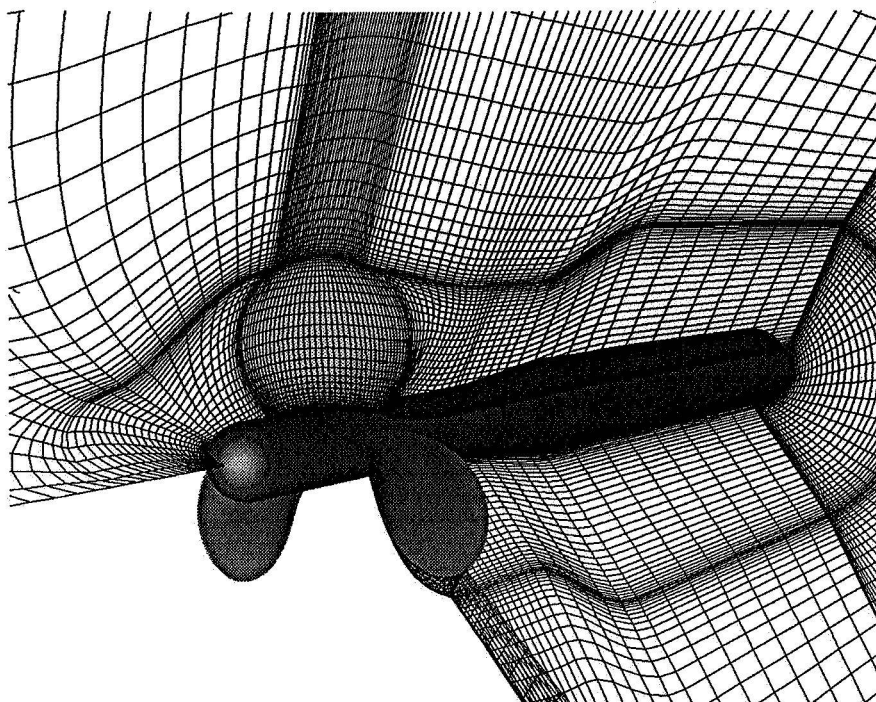


Figure 7 3-block grid of marine propeller 4119

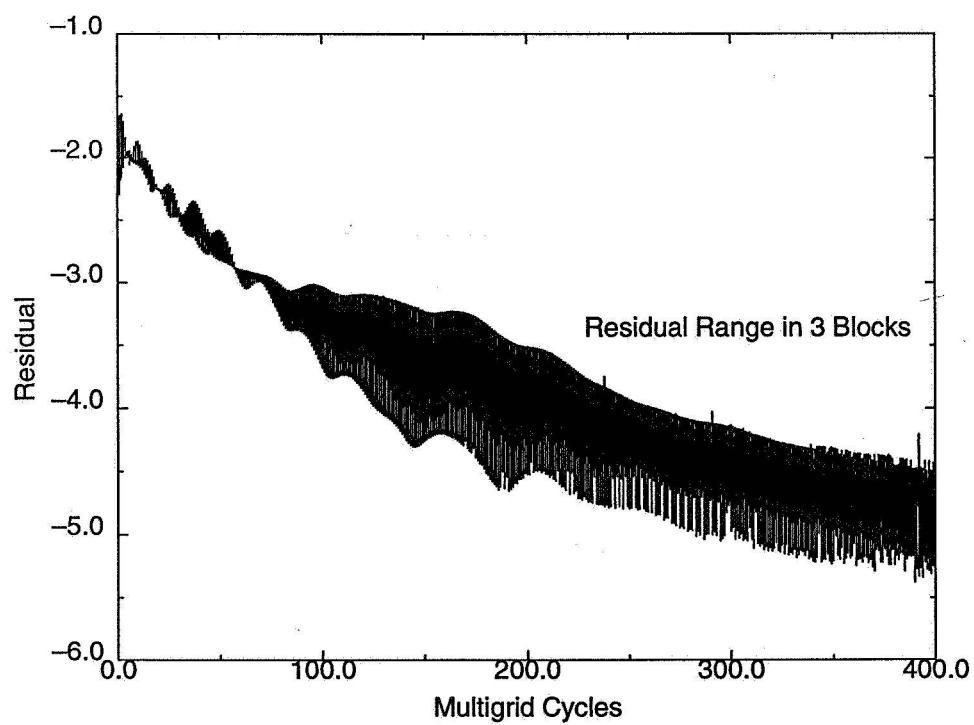


Figure 8 Convergence history of 4-level multigrid solution of a marine propeller 4119 in rotating frame at CFL=5

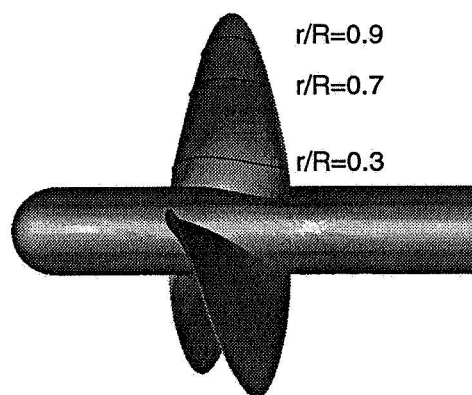
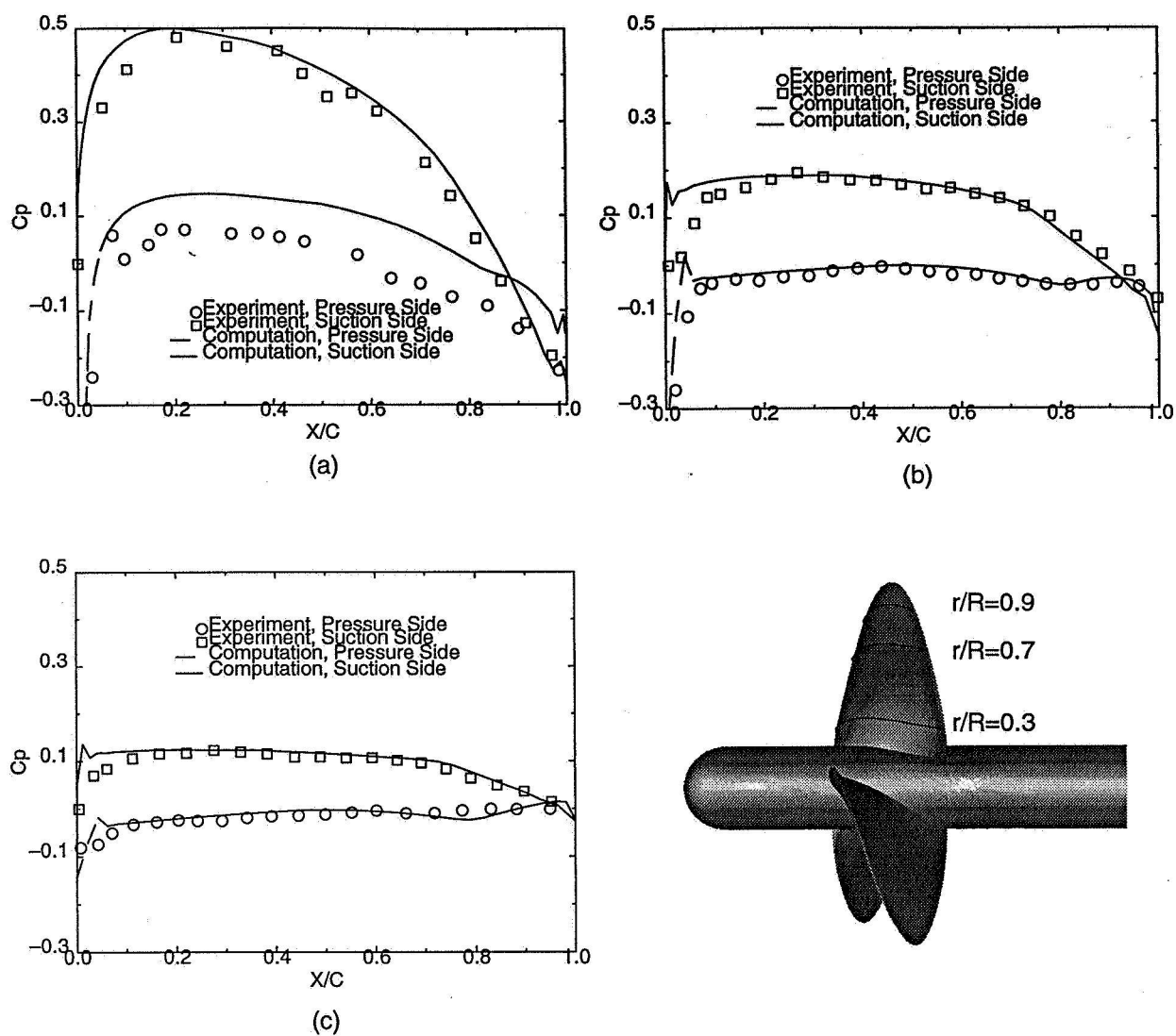
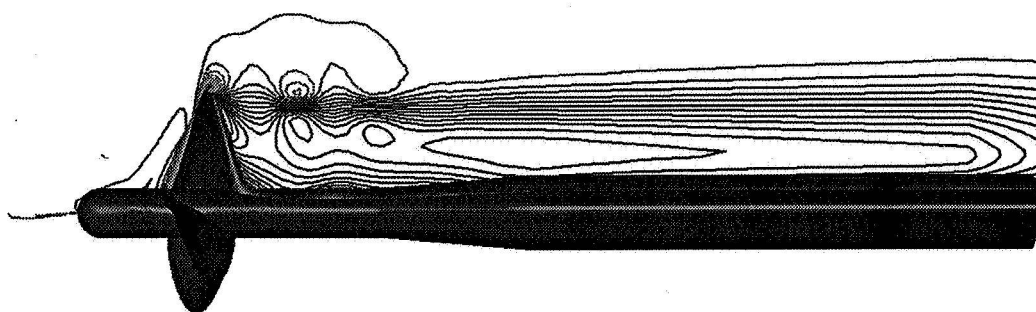
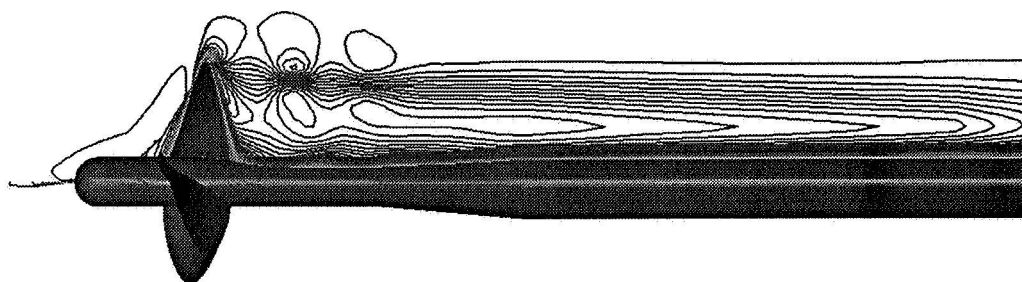


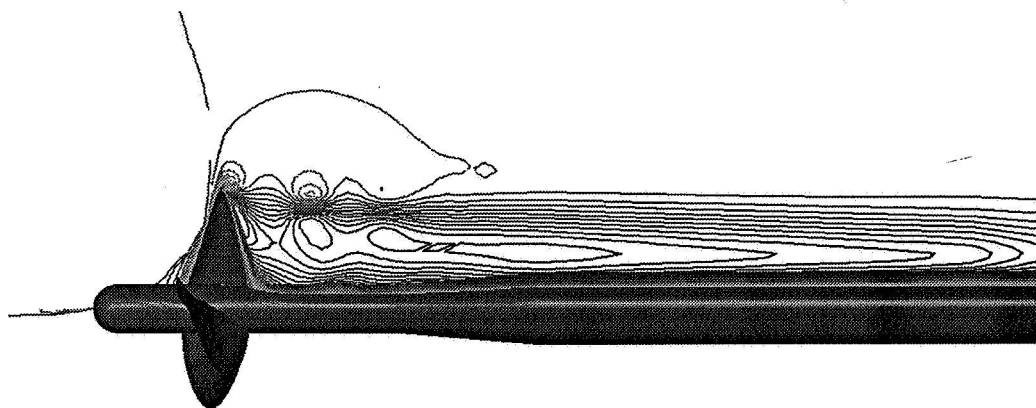
Figure 9 Computed (in rotating frame) and measured pressure coefficients on the blade surfaces at (a) $r/R=0.3$, (b) $r/R=0.7$, (c) $r/R=0.9$



(a)

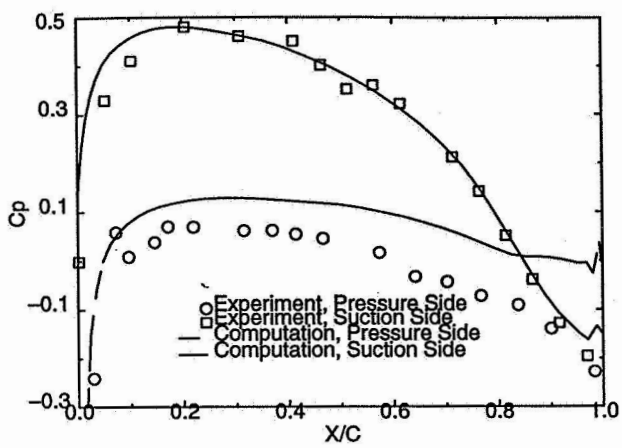


(b)

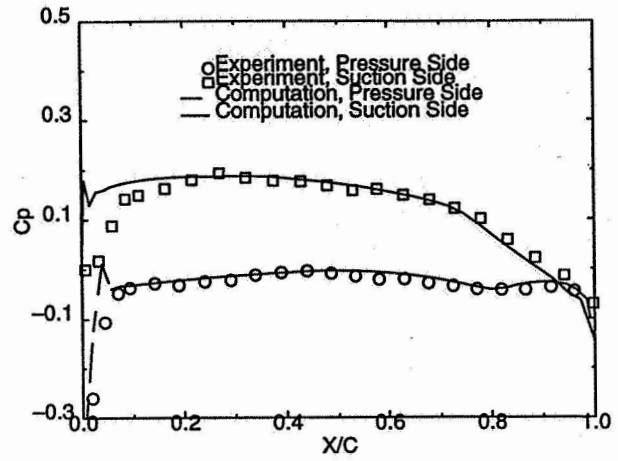


(c)

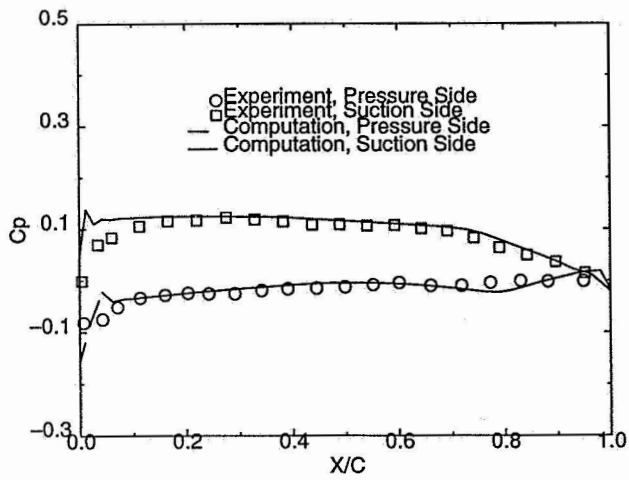
Figure 10 Computed u -velocity contours (a) in rotating frame,
(b) in absolute frame with 1 multigrid cycle,
(c) in absolute frame with 2 multigrid cycles



(a)



(b)



(c)

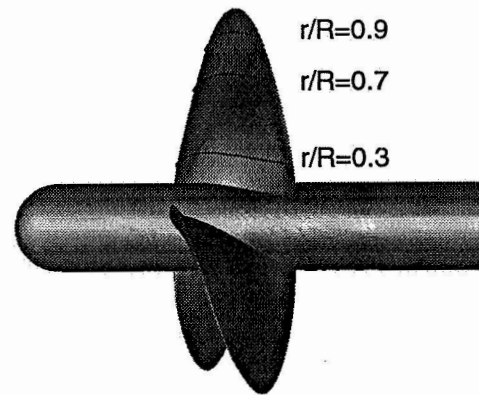


Figure 11 Computed (in absolute frame) and measured pressure coefficients on the blade surfaces at (a) $r/R=0.3$, (b) $r/R=0.7$, (c) $r/R=0.9$

	Thrust Coefficient	Torque Coefficient
Experimental Data	0.146	0.028
Computation in Rotating Frame	0.1497	0.0254
Computation in Absolute Frame	0.1498	0.0256

Table 1. Measured and computed thrust coefficient and torque coefficient